AIAA AVIATION Forum
12-16 June 2023, San Diego, CA and Online
AIAA AVIATION 2023 Forum

10.2514/6.2023-4279

Feasibility Study of Deflected Slipstream Airfoil for VTOL Hover Enabled by CoFlow Jet

Gecheng Zha *
CoFlow Jet, LLC
PO Box 248661, Coral Gables, FL 33124

Abstract

This paper conducts a feasibility study of deflected slipstream (DS) airfoil enabled by coflow jet (CFJ) active flow control for VTOL hover based on 2D numerical simulation. Such a DS-CFJ system can potentially provide a fully electric powered Advanced Air Mobility (AAM) platform with distributed propulsors and CFJ actuators. It would have the advantages to eliminate tilting wings, tilting rotors, and separate lift-plus-cruise propulsors, and has the potential to improve cruise efficiency, smooth transition, safety, weight reduction, noise mitigation, reliability, maintainability, and passenger acceptance.

The in house high order FASIP CFD code is employed with one equation Spalart-Allmaras turbulence model. The baseline DS airfoil is the double slotted configuration designed by Kuhn and Draper in NACA based on NACA 0015 airfoil. The CFD simulation is validated with the test data of the baseline DS airfoils with several deflection angles. Good agreement with the experiment is obtained for the 2D simulation. The DS-CFJ airfoil is created based on the baseline airfoil. For a single plain flap configuration with a 60% flap chord and 85° deflection angle, applying CFJ on the flap can turn the horizontal slipstream form the propeller vertically downward with fully attached flow. The best performance is to place the propeller a little upward with the airfoil leading edge aligned with the lower 1/4 diameter position of the propeller, named as Case D242 in this paper. The 2D D242 configuration achieves a 90° flow turning and about the same hover efficiency as a vertical rotor facing upward. It obtains 99.3% of the Figure of Merit for DS-CFJ, FM_{DS}. FM_{DS} is defined to compare the total power required of a DS-CFJ system, which includes the CFJ viscous loss and energy consumption, with the power of a vertical rotor disk facing upward for the same amount of total lift. The high efficiency is attributed to the favorable position of the propeller mounted 1/4R upward, the low energy expenditure of CFJ, and the system benefit that absorbs the energy expenditure of CFJ as the system exergy gain. The total lift of D242 is 5.7% higher than the full propeller thrust due to the enhanced momentum of the deflected slipstream by the CFJ. The CFJ power consumption is about 8.7% of the total power. Attributed to the lift contribution of CFJ, the reduced propeller lift and power required would reduce its disk loading and power loading, resulting in potentially increased propeller efficiency and reduced noise. A slotted flap has a lower efficiency than the plain flap. The configuration with the propeller center aligned with the airfoil leading edge, Case D245, also decreases the efficiency to 92.6%. All the injection Mach number is no greater than 0.27 and can be further reduced with optimization. Thus the jet noise is not expected to be a serious concern with the jet Mach number below the noise limit of 0.3 - 0.5. Since a DS-CFJ system avoids the separated flow and large turbulent wakes caused by vertical rotor downwash interaction with the airframe, the broadband noise is expected to be lower.

This paper shows that a 2D deflected slipstream enabled by coflow jet active flow control appears to be feasible to achieve a similar hover efficiency to the conventional vertical rotor with the same size and total lift. The performance penalty due to 3D effect needs to be further studied. This study lays a foundation for further 3D study and experimental verification in the next step.

Nomenclature

A Propeller disk area

* Ph.D., President, AIAA Associate Fellow, Professor, U. of Miami

AR	Wing aspect ratio
AoA	Angle of attack
CFJ	Co-flow jet
C	Profile chord
C_L	Lift coefficient $L/(q_\infty S)$
C_D	Drag coefficient $D/(q_\infty S)$
C_m	Pitching moment coefficient $M_{c/4}/(q_\infty Sc)$
C_μ	Jet momentum coef. $\dot{m}_j U_j/(q_\infty S)$
$(C_L/C_D)_c$	CFJ airfoil corrected aerodynamic efficiency $C_L/(C_D + P_c)$
$(C_L^2/C_D)_c$	CFJ airfoil corrected productivity efficiency $C_L^2/(C_D + P_c)$
D	Drag
DS	Deflected Slipstream
DL	Disk loading, thrust of the actuator disk/actuator disk area
DL_c	Disk loading coefficient
FM_{DS}	Figure of Merit for the DS system
L	Lift
LE	Leading Edge
M	Mach number
P_{tot}	Total power of the DS-CFJ system
P_c	CFJ power coefficient $P/(q_\infty S V_\infty)$
P_P	Propeller actuator power coefficient $\frac{2}{\rho V_\infty^3 S}\sqrt{\frac{F^3}{2\rho A}}$
PL	Power loading, power/lift
PL_c	Power loading coefficient
ΔP	Pressure percentage increase across the propeller actuator disk
p	Static pressure
q	Dynamic pressure $0.5\,\rho\,U^2$
R	Propeller disk radius
S	Wing planform area
T	Thrust
TE	Trailing Edge
U	Flow velocity
$_j$	Jet conditions
δ	Flap deflection angle, deg
β	Resultant force angle of the DS-CFJ system about horizontal
$d\beta$	Resultant force angle variation range
ρ	Air density
$\dot{m}$	Mass flow
Γ	Total pressure ratio of the CFJ injection to suction
∞	Free stream conditions

1 Introduction

Vertical takeoff and landing aircraft is an important area of aviation for their special features of runway independence. The current development of urban air mobility enhances the demands of advanced VTOL technologies. Electric vertical takeoff/landing (eVTOL) [1] fixed wing aircraft are playing a critical role in the transformation of urban transportation and eCommerce goods shipment. The current first generation (1G) eVTOL technology is based on conventional rotorcraft aerodynamic principles with vertical propellers facing upward for hover, including tiltrotors (e.g. V-280, V-22, Joby), tiltwings (e.g. Hiller X-18, Airbus Vahana18), and lift-plus-cruise (e.g. SB-1, Wisk). The 1G eVTOL does have a significant advantage over conventional rotorcraft by using distributed propulsors of multiple small

propellers, which benefit noise mitigation, increase efficiency, and enable higher cruise speed using fixed wing configurations.

Conventional rotorcraft technology uses vertical propellers to lift up vehicles by exhausting flow downward (downwash), which has high hover efficiency. However, if the air vehicle requires a forward flight mission, a vertical propeller would have the disadvantage of low cruise efficiency. In general, rotorcraft have the following three limitations: 1) High complexity: A tiltrotor or tiltwing must be used to rotate the propellers to face forward direction. Such a system needs a complex mechanical system with high weight penalty. A complex system may be more prone to reliability issues. Transition between hover and cruise could also pose a challenge as it must ensure sufficient lift and trim when the full cruise speed is not yet achieved (takeoff) or is aborted (landing). 2) Noise: The noise level at cruise could be controlled by reduced disk loading and rotor tip speed. However, the broadband noise generated at hover due to flow separation caused by the rotor downwash-wing interaction and its turbulent wakes is significant and difficult to avoid. 3) Range: A rotorcraft based VTOL vehicle in general has low mission efficiency that affects the range. This is due to their weight and drag penalty associated with some major components only used for hover instead of the entire flight envelop, such as the lift-plus propellers/struts and the heavy rotor or wing tilting system.

The motivation of this paper is to seek an effective deflected slipstream technology that has the potential to improve VTOL aircraft mission efficiency and mitigate hover noise by avoiding using conventional vertical rotor lifting principle.

1.1 Deflected Slipstream VTOL

The deflected slipstream (DS) concept pioneered by Kuhn and Draper in NACA in the late 1950's [2–4] generates hover lift by deflecting the slipstream from the propeller downward using a deflected flap. Once airborne, the flap is retracted for high-speed cruise. Fig. 1 illustrates the concept of Kuhn and Draper [3]. An effective DS wing system would not need to use tiltwings, tiltrotors or lift-plus configurations to simplify the system.

The deflected slipstream concept can be explained by a control volume analysis based on the sketch in Fig. 2, which illustrates a running propeller and a flapped airfoil immersed in a static field enclosed by a rectangle control volume with two horizontal boundaries and two vertical boundaries. The far field boundaries are far enough that the velocity is zero except at the lower boundary, which has a slipstream deflected by the flap exciting the boundary at an averaged velocity $\mathbf{V_{DS}}$ and flow angle β about the horizontal. Applying fluid mechanics momentum equation on the control volume with a simply connected domain surrounding the airfoil will give,

$$\mathbf{F} = \iint_s (\rho \mathbf{V} \cdot d\mathbf{S})\mathbf{V} = -\dot{m}\mathbf{V_{DS}} \tag{1}$$

where $\mathbf{F}$ is the resultant force acting on the airfoil, ρ and $\mathbf{V}$ are the flow density and velocity on the control volume boundaries respectively, and $\dot{m}$ is the mass flow of the slipstream crossing the lower boundary. Eq. (1) means that the resultant force acting on the airfoil is in the opposite direction of the deflected slipstream velocity $\mathbf{V_{DS}}$. If $\beta \neq 90°$, the airfoil has a lift and thrust (or drag) component. If β is 90°, the resultant force $\mathbf{F}$ becomes all lift. This is how the DS system generates the lift without tilting the rotor, but by deflecting the flap. Eq. (1) indicates that increasing the deflected slipstream mass flow and velocity will increase the resultant force. For vertical takeoff and landing hover maneuver, it is desirable to have $\beta = 90°$, but a range such as $\beta = 90° \pm d\beta$ with $d\beta < 10°$ may also function with typical surrounding environment. For cruise, the propeller generates thrust with $\beta = 0°$. The variation between lift and thrust for a DS system is controlled by varying the deflection angle of the flaps.

The deflected slipstream principle seems simple and clear, but turning the horizontal slipstream from the propeller vertically downward is very challenging because flow suffers severe separation when the flap angle is large. A double-plain flap system tested by Kuhn and Draper [2] was able to deflect the flow by 45°. A double-slotted flap [3] increased the deflection to 63°. Such a flow deflection is not sufficient for hover, in particular with the ground effect. The efforts using DS for VTOL were abandoned in 1960's.

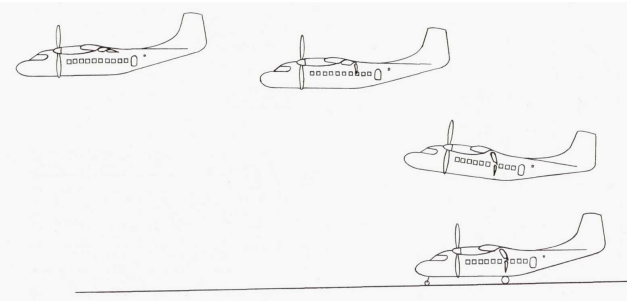

Figure 1: VTOL based on a deflected slipstream system [3].

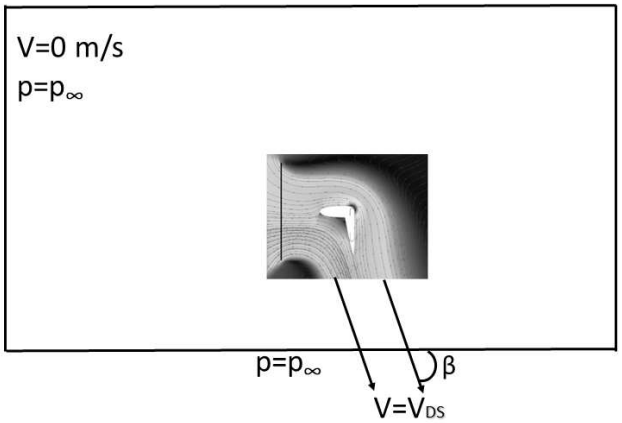

Figure 2: Control volume analysis of a deflected slipstream system.

Antcliff et al at NASA [1] recently revisited the DS concept and suggested using CoFlow Jet (CFJ) active flow control (AFC) to enhance the flow turning. They envision that it "could provide benefits in cruise efficiency, weight, noise, reliability, and maintainability, and offer safer transition characteristics" [1].

It is appealing if the coflow jet AFC can achieve the following three features: 1) turn the slipstream 90° with fully attached flow; 2) have low energy expenditure that a DS-CFJ achieves a similar hover efficiency to a vertical rotor; 3) increase the cruise efficiency. The third feature is addressed in [5–10] for regular CFJ airfoils with the injection slot closer to the airfoil leading edge. This paper is to focus on addressing the feasibility of the first and second feature. Such a DS VTOL system would have all the major components used in entire flight envelop including hover, climb, cruise, and extreme maneuver, instead of being only used at one point of the flight envelop. It would reduce weight and enable a high mission efficiency. It would also avoid the hover downwash interaction with the aircraft wings and fuselage to mitigate the broad band noise caused by flow separation and large turbulent wakes. The transition between hover and cruise can be made smoother and simplified since the major propulsors are fixed in the forward flight direction. Retracting flaps is a mature technology that is already widely used in aircraft, in particular if the flaps can adopt a simple configuration such as single plain flaps.

1.2 CoFlow Jet (CFJ) Active Flow Control

CFJ is a zero-net-mass-flux (ZNMF) active flow control technique recently developed by Zha and his team [6, 7, 11–24]. As illustrated in Fig. 3, a small amount of mass flow is drawn into the airfoil near the trailing edge, pressurized and energized by a micro-compressor system inside the airfoil, and then injected near the leading edge in the direction tangent to the main flow. CFJ achieves ultra-high lift coefficient exceeding the theoretical limit [6], thrust generation, and very high stall angle of attack (e.g., 70°) with low energy expenditure.

Fig. 4 is the photo of the CFJ-NACA6421 airfoil recently tested in wind tunnel with 5 compressors embedded inside the airfoil along the span [25]. The C_{Lmax} of 8.6 is achieved as shown in the drag polar in Fig. 5, which is far greater than the theoretical limit of C_{Lmax}=7.6 for this airfoil. Fig. 5 also shows that the CFJ airfoil generates very high thrust up to $C_D = -1.0$. The operating range of CFJ airfoil without stall is dramatically increased. The CFJ airfoil has very low energy expenditure, which is the unique feature enabling CFJ wing to enhance productivity efficiency at cruise even when the flow is at its most favorable condition at low angle of attack [5, 8–10].

Xu et al [23, 26] analyze the mechanism of coflow wall jet and indicate that it is most efficient and effective to apply CFJ in adverse pressure gradient (APG) region, which would have the injection placed at the location of separation onset and the entire CFJ immersed in the APG area. Xu and Zha [24] apply CFJ on an aircraft control surface flap and find that it is much more efficient and effective than applying the CFJ in the front part due to being immersed in the APG region. McBreen et al. [27] demonstrate numerically that the CFJ is able to overcome an adverse pressure gradient 3 orders of magnitude higher

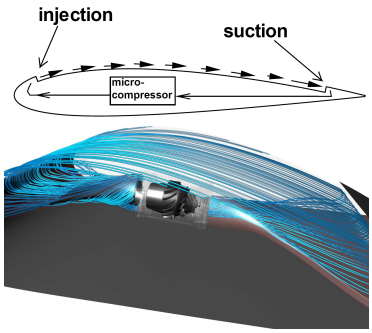

Figure 3: *CFJ airfoil concept and micro-compressor embedded.*

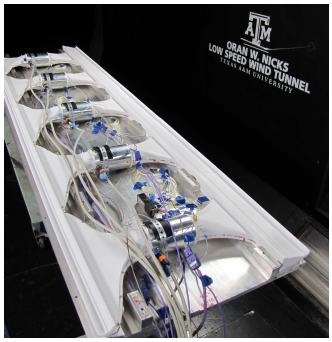

Figure 4: *Photo of the wind tunnel tested airfoil with 5 compressors embedded.*

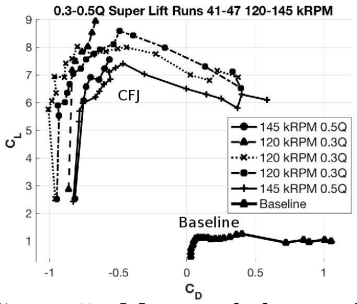

Figure 5: Measured drag polar of the CFJ and baseline airfoil [25].

than the baseline configuration that has no flow control. Xu and Zha [24] conduct exergy analysis, which shows that the energy consumed by CFJ active flow control (AFC) is fully absorbed by the controlled flow as system exergy gain due to the ZNMF. The CFJ AFC is able to benefit the system efficiency attributed to the exergy benefit and improved flow performance (e.g. flow separation removal).

The purpose of this paper is to numerically demonstrate that the coflow jet is feasible to deflect the slipstream of a propeller by an airfoil with a simple plain flap at low energy expenditure. This will lay a foundation for further development of the DS-CFJ technology.

2 CFJ and Hover Parameters

The following are the parameters to define the performance of the CFJ airfoil and the deflected slipstream system. The hover simulation is at static condition with freestream velocity of 0, which can not be used to normalize some aerodynamic parameters described below. An arbitrarily chosen reference condition with Mach 0.04 and standard atmospheric condition is used in this study.

2.1 Lift and Drag Calculation

The momentum and pressure at the injection and suction slots produce a reactionary force that needs to be included in CFD simulation. Zha et al. [11] give the following formulations to calculate the lift and drag for a CFJ airfoil based on a control volume analysis.

$$F_{x_{cfj}} = (\dot{m}_j V_{j1} + p_{j1} A_{j1}) * cos(\theta_1 - \alpha) - (\dot{m}_j V_{j2} + p_{j2} A_{j2}) * cos(\theta_2 + \alpha) \tag{2}$$

$$F_{y_{cfj}} = (\dot{m}_{j1} V_{j1} + p_{j1} A_{j1}) * sin(\theta_1 - \alpha) + (\dot{m}_{j2} V_{j2} + p_{j2} A_{j2}) * sin(\theta_2 + \alpha) \tag{3}$$

where the subscripts 1 and 2 stand for the injection and suction respectively, and θ_1 and θ_2 are the angles between the injection and suction slot's surface and a line normal to the airfoil chord. α is the angle of attack.

The total lift and drag on the airfoil can then be expressed as:

$$D = R'_x - F_{x_{cfj}} \tag{4}$$

$$L = R'_y - F_{y_{cfj}} \tag{5}$$

where R'_x and R'_y are the surface integral of pressure and shear stress in x (drag) and y (lift) direction excluding the internal ducts of injection and suction. For CFJ wing simulations, the total lift and drag are calculated by integrating Eqs.(4) and (5) in the spanwise direction.

2.2 Jet Momentum Coefficient

The jet momentum coefficient C_μ is a parameter used to quantify the jet intensity. It is defined as:

$$C_\mu = \frac{\dot{m} V_j}{\frac{1}{2}\rho_\infty {V_\infty}^2 S} \tag{6}$$

where $\dot{m}$ is the injection mass flow, V_j is the mass-averaged injection velocity, ρ_∞ and V_∞ denote the free stream reference density and velocity, and S is the planform area.

2.3 Power Coefficient

CFJ is implemented by mounting a pumping system inside the wing that withdraws air from the suction slot and blows it into the injection slot. The power consumption is determined by the jet mass flow and total enthalpy change as the following:

$$P_{CFJ} = \dot{m}(H_{t1} - H_{t2}) \tag{7}$$

where H_{t1} and H_{t2} are the mass-averaged total enthalpy in the injection cavity and suction cavity respectively, P is the Power required by the pump and $\dot{m}$ the jet mass flow rate. Introducing P_{t1} and P_{t2} the mass-averaged total pressure in the injection and suction cavity respectively, the pump efficiency η, and the total pressure ratio of the pump $\Gamma = \frac{P_{t1}}{P_{t2}}$, the power consumption is expressed as:

$$P_{CFJ} = \frac{\dot{m} C_p T_{t2}}{\eta}(\Gamma^{\frac{\gamma-1}{\gamma}} - 1) \tag{8}$$

where γ is the specific heat ratio equal to 1.4 for air. The power coefficient for CFJ is expressed as:

$$P_c = \frac{P_{CFJ}}{\frac{1}{2}\rho_\infty V_\infty^3 S} \tag{9}$$

In order to compare the efficiency of a CFJ airfoil with that of a conventional airfoil, a corrected aerodynamic efficiency $(L/D)_c$ is introduced, which takes into consideration of the power needed for the CFJ [18] as the following:

$$(\frac{C_L}{C_D})_c = \frac{L}{D + \frac{P}{V_\infty}} = \frac{C_L}{C_D + P_C} \tag{10}$$

where V_∞ is the free stream velocity, P is the CFJ pumping power, L and D are the lift and drag generated by the CFJ airfoil, and C_L, C_D and P_C are the coefficient of lift, drag and CFJ pumping power. The $(L/D)_c$ incorporates the CFJ power consumed into the drag of the airfoil.

2.4 Disk Loading and Power Loading

For rotorcraft aerodynamics, the ideal power coefficient for the propeller based actuator disk momentum theory at static condition is:

$$P_p = \frac{2}{\rho_\infty V_\infty^3 S}\sqrt{\frac{L^3}{2\rho A}} \tag{11}$$

where A is the actuator disk area; L is the total force produced by the propeller actuator normal to the propeller disk. L would be the lift for a vertical rotor or thrust for a horizontal rotor. The same reference parameters for the airframe aerodynamic parameters are used to normalize the rotor parameters to be consistent.

Disk loading and power loading are used to describe rotorcraft VTOL performance. The disk loading (DL) is defined as

$$DL = L/A \tag{12}$$

The disk loading is closely related to the noise produced by a rotor. A higher disk loading will in general generate louder noise. The power loading (PL) for a propeller disk at static hovering condition is defined as

$$PL = P/L \tag{13}$$

where P is the propeller power used to generate the lift L. The power loading indicates the power required per unit lift for rotorcraft. The disk loading and power loading coefficients are defined as follows:

$$DL_c = \frac{DL}{\frac{1}{2}\rho V_\infty^2} = \frac{C_L}{A_c} \tag{14}$$

where $C_L = L/(0.5\rho V^2 S)$, $A_c = A/S$, A is the disk area and S is the wing planform area.

$$PL_c = \frac{PL}{V_\infty} = \frac{P_p}{C_L} \tag{15}$$

The actuator DL and PL has the following relations in hover static condition:

$$PL = \sqrt{DL\frac{1}{2\rho}} \tag{16}$$

$$PL_c = \frac{\sqrt{DL_c}}{2} \tag{17}$$

2.5 Figure of Merit for DS-CFJ Hover

To compare the efficiency of the DS-CFJ hover system with a vertical rotor with the same total lift and disk size, we adopt a parameter FM_{DS} similar to the figure of merit (FM) of rotorcraft below:

$$FM_{DS} = \frac{P_p}{P_{DS-CFJ}} = \frac{P_p}{P_{prop} + P_c} \tag{18}$$

where P_p is the ideal power coefficient required by a vertical rotor disk that generates the same lift of the DS-CFJ system with the same rotor disk size based on Eq. (11). The total power required by the DS-CFJ system P_{DS-CFJ} is the summation of the propeller power P_{prop} and the CFJ power P_c.

To isolate the CFJ effect in the parameter FM_{DS}, the propeller power P_{prop} of the DS-CFJ system is also calculated based on the disk theory formulation Eq. (11), which uses the disk loading determined by the pressure rise imposed on the disk as the boundary condition. The CFJ power required P_c is determined by Eq. (8) and (9). The power coefficient P_c studied in this paper includes all the viscous effect of the DS-CFJ system governed by Reynolds averaged Navier-Stokes (RANS) equations, but the CFJ actuator efficiency in Eq. 8 is set to be 100% to consider only the power required to achieve the AFC performance. Currently, the efficiency of a micro-compressor with the diameter of 64 mm we have designed is slightly more than 84% [28]. In an integrated system with a CFJ airfoil and a micro-compressor actuator, the micro-compressor efficiency is dropped to 76%-80% [29, 30]. Such efficiency range is similar to the typical figure of merit of vertical rotors. With more design optimization, a higher micro-compressor efficiency is achievable. If FM_{DS} is 1, it means that the DS-CFJ system has the same hover efficiency to a vertical rotor with the same total lift and disk size.

3 Numerical Approaches

3.1 Governing Equations

The governing equations for the CFD simulation are the unsteady Reynolds averaged Navier-Stokes equations (URANS) with one equation Spalart-Allmaras turbulence model [31], which are solved in a

fully coupled manner using an implicit unfactored Gauss-Seidel line iteration to achieve a high convergence rate. In generalized coordinate system, the conservative form of the equations are given as the following:

$$\frac{\partial Q}{\partial t}+\frac{\partial \mathbf{E}}{\partial \xi}+\frac{\partial \mathbf{F}}{\partial \eta}+\frac{\partial \mathbf{G}}{\partial \zeta}=\frac{1}{\mathrm{Re}}\left(\frac{\partial \mathbf{R}}{\partial \xi}+\frac{\partial \mathbf{S}}{\partial \eta}+\frac{\partial \mathbf{T}}{\partial \zeta}+\mathbf{D}\right), \tag{19}$$

where,

$$Q=\frac{1}{\mathrm{J}}\begin{bmatrix}\rho\\ \rho u\\ \rho v\\ \rho w\\ \rho e\\ \rho\tilde{\nu}\end{bmatrix}, \tag{20}$$

$$\mathbf{E}=\begin{bmatrix}\rho U\\ \rho uU+l_xp\\ \rho vU+l_yp\\ \rho wU+l_zp\\ (\rho e+p)\,U-l_tp\\ \rho\tilde{\nu}U\end{bmatrix},\ \mathbf{F}=\begin{bmatrix}\rho V\\ \rho uV+m_xp\\ \rho vV+m_yp\\ \rho wV+m_zp\\ (\rho e+p)\,V-m_tp\\ \rho\tilde{\nu}V\end{bmatrix}, \tag{21}$$

$$\mathbf{G}=\begin{bmatrix}\rho W\\ \rho uW+n_xp\\ \rho vW+n_yp\\ \rho wW+n_zp\\ (\rho e+p)\,W-n_tp\\ \rho\tilde{\nu}W\end{bmatrix},\ \mathbf{R}=\begin{bmatrix}0\\ l_k\tau_{xk}\\ l_k\tau_{yk}\\ l_k\tau_{zk}\\ l_k\beta_k\\ \frac{\rho}{\sigma}\left(\nu+\tilde{\nu}\right)\left(\mathbf{l}\bullet\nabla\tilde{\nu}\right)\end{bmatrix}, \tag{22}$$

$$\mathbf{S}=\begin{bmatrix}0\\ m_k\tau_{xk}\\ m_k\tau_{yk}\\ m_k\tau_{zk}\\ m_k\beta_k\\ \frac{\rho}{\sigma}\left(\nu+\tilde{\nu}\right)\left(\mathbf{m}\bullet\nabla\tilde{\nu}\right)\end{bmatrix},\ \mathbf{T}=\begin{bmatrix}0\\ n_k\tau_{xk}\\ n_k\tau_{yk}\\ n_k\tau_{zk}\\ n_k\beta_k\\ \frac{\rho}{\sigma}\left(\nu+\tilde{\nu}\right)\left(\mathbf{n}\bullet\nabla\tilde{\nu}\right)\end{bmatrix}, \tag{23}$$

$$D=\frac{1}{\mathrm{J}}\begin{bmatrix}0\\ 0\\ 0\\ 0\\ 0\\ S_\nu\end{bmatrix}, \tag{24}$$

where

$$\beta_k=u_i\tau_{ki}-q_k, \tag{25}$$

$$\begin{aligned}S_\nu=\rho C_{b1}\left(1-f_{t2}\right)\tilde{S}\tilde{\nu}+\tfrac{1}{\mathrm{Re}}\Big[-\rho\left(C_{w1}f_w-\tfrac{C_{b1}}{\kappa^2}f_{t2}\right)\left(\tfrac{\tilde{\nu}}{d}\right)^2\\ +\tfrac{\rho}{\sigma}C_{b2}\left(\nabla\tilde{\nu}\right)^2-\tfrac{1}{\sigma}\left(\nu+\tilde{\nu}\right)\nabla\tilde{\nu}\bullet\nabla\rho\Big]+\mathrm{Re}\left[\rho f_{t1}\left(\Delta U\right)^2\right].\end{aligned} \tag{26}$$

In the equations above, U, V and W are the contravariant velocities in ξ, η and ζ directions.

$$\begin{aligned}U&=l_t+\mathbf{l}\bullet\mathbf{V}=l_t+l_xu+l_yv+l_zw,\\ V&=m_t+\mathbf{m}\bullet\mathbf{V}=m_t+m_xu+m_yv+m_zw,\\ W&=n_t+\mathbf{n}\bullet\mathbf{V}=n_t+n_xu+n_yv+n_zw,\end{aligned} \tag{27}$$

where $\mathbf{V} = (u, v, w)$ is the velocity vector, $\mathbf{l}$, $\mathbf{m}$, $\mathbf{n}$ are the normal vectors on ξ, η, ζ surfaces with their magnitudes equal to the elemental surface area and pointing to the directions of increasing ξ, η, ζ.

$$\mathbf{l} = \frac{\nabla\xi}{\mathrm{J}}\mathrm{d}\eta\mathrm{d}\zeta,\ \mathbf{m} = \frac{\nabla\eta}{\mathrm{J}}\mathrm{d}\xi\mathrm{d}\zeta,\ \mathbf{n} = \frac{\nabla\zeta}{\mathrm{J}}\mathrm{d}\xi\mathrm{d}\eta. \tag{28}$$

l_t, m_t, n_t stand for the grid moving velocities and are defined as

$$l_t = \frac{\xi_t}{\mathrm{J}}\mathrm{d}\eta\mathrm{d}\zeta,\ m_t = \frac{\eta_t}{\mathrm{J}}\mathrm{d}\xi\mathrm{d}\zeta,\ n_t = \frac{\zeta_t}{\mathrm{J}}\mathrm{d}\xi\mathrm{d}\eta. \tag{29}$$

When the grid is stationary, $l_t = m_t = z_t = 0$.

Since $\Delta\xi = \Delta\eta = \Delta\zeta = 1$ are used in the current discretization, Eqs.(28) and (29) are written as the following in the solver,

$$\mathbf{l} = \frac{\nabla\xi}{\mathrm{J}},\ \mathbf{m} = \frac{\nabla\eta}{\mathrm{J}},\ \mathbf{n} = \frac{\nabla\zeta}{\mathrm{J}}, \tag{30}$$

$$l_t = \frac{\xi_t}{\mathrm{J}},\ m_t = \frac{\eta_t}{\mathrm{J}},\ n_t = \frac{\zeta_t}{\mathrm{J}}. \tag{31}$$

The shear-stress τ_{ik} and total heat flux q_k in Cartesian Coordinate can be expressed as

$$\tau_{ik} = (\mu + \mu_t)\left[\left(\frac{\partial u_i}{\partial x_k} + \frac{\partial u_k}{\partial x_i}\right) - \frac{2}{3}\delta_{ik}\frac{\partial u_j}{\partial x_j}\right], \tag{32}$$

$$q_k = -\left(\frac{\mu}{\mathrm{Pr}} + \frac{\mu_t}{\mathrm{Pr}_t}\right)\frac{\partial T}{\partial x_k}, \tag{33}$$

where, Pr is the Prandtl number, Pr_t is the turbulent Prandtl number, μ is the molecular viscosity determined by Sutherland law and μ_t is the turbulent viscosity determined by the S-A model [31]

$$\mu_t = \rho\tilde{\nu}f_{v1}. \tag{34}$$

The kinematic viscosity ν is defined as

$$\nu = \frac{\mu}{\rho}. \tag{35}$$

In Eqs.(22), (23), (25), (32) and (33), the repeated subscripts i or k represent the coordinates x, y and z following Einstein summation convention. Eqs.(32) and (33) are transformed to generalized coordinate system in computation.

The sixth equation of the governing equations (19)-(24) is the S-A one equation turbulence model [31]. The functions in the equation are given as

$$\begin{aligned}
&f_{v1} = \tfrac{\chi^3}{\chi^3 + C_{\nu 1}^3},\ \chi = \tfrac{\tilde{\nu}}{\nu},\\
&\tilde{S} = S + \tfrac{\tilde{\nu}}{\mathrm{Re}\kappa^2 d^2} f_{v2},\ f_{v2} = 1 - \tfrac{\chi}{1+\chi f_{v1}},\\
&f_w = g\left[\tfrac{1+C_{w3}^6}{g^6 + C_{w3}^6}\right]^{\frac{1}{6}},\ g = r + C_{w2}\left(r^6 - r\right),\ r = \tfrac{\tilde{\nu}}{\mathrm{Re}\tilde{S}\kappa^2 d^2},\\
&f_{t1} = C_{t1} g_t exp\left[-C_{t2}\tfrac{\omega_t^2}{\Delta U^2}\left(d^2 + g_t^2 d_t^2\right)\right],\ g_t = min\left(0.1, \tfrac{\Delta U}{\omega_t \Delta x_t}\right),\\
&f_{t2} = C_{t3} exp\left(-C_{t4}\chi^2\right),
\end{aligned} \tag{36}$$

where, $S = \sqrt{\left(\frac{\partial w}{\partial y} - \frac{\partial v}{\partial z}\right)^2 + \left(\frac{\partial u}{\partial z} - \frac{\partial w}{\partial x}\right)^2 + \left(\frac{\partial v}{\partial x} - \frac{\partial u}{\partial y}\right)^2}$ is the magnitude of vorticity, which is also transformed to generalized coordinate system, ω_t is the wall vorticity at the wall boundary layer trip location, d is the distance to the closest wall. d_t is the distance of the field point to the trip location, ΔU is the difference of the velocities between the field point and the trip location, Δx_t is the grid spacing along the wall at the trip location.

3.2 Navier-Stokes Equations Solver

The in-house high order CFD code Flow-Acoustics-Structure Interaction Package (FASIP) is used to solve the 2D unsteady-Reynolds averaged Navier-Stokes equations. A 3rd order WENO scheme for the inviscid flux [32–35] and a 4th order central differencing for the viscous terms [33, 34] are employed to discretize the Navier-Stokes equations. The low diffusion E-CUSP scheme suggested by Zha et al. [35] based on the Zha-Bilgen flux vector splitting [32] is utilized with the WENO scheme to evaluate the inviscid fluxes. All the simulations in this study are conducted as unsteady time accurate simulations. The second order time-accurate implicit time marching method with pseudo time and Gauss-Seidel line relaxation is used to achieve a fast convergence rate [36, 37]. Parallel computing is implemented to save wall clock simulation time [38]. The FASIP code is intensively validated for CFJ simulations [6,11,13,14,18,20,22,23,38,39]. The time-averaged results are presented after the flows and all the aerodynamic forces become dynamically stable.

3.3 Boundary Conditions

The 3rd order accuracy no slip condition is enforced on the solid surface with the wall treatment suggested in [33] to achieve the flux conservation on the wall. A 2D computational mesh is shown in Fig. 6. Total pressure, total temperature and flow angles are specified at the injection duct inlet, as well as the upstream portion of the far field. For the static condition, the static pressure at the downstream farfield is set to be equal to the total pressure at upstream far field. Constant static pressure is applied at the suction duct outlet as well as the downstream portion of the far field. The total mesh size is 91,440 for all 2D cases, split into 23 blocks for the parallel computation. The domain size is about 500 chords away from the airfoil to ensure a solid convergence at the static flow conditions. The actuator disk BC is modeled as a flat surface, across which the static pressure is increased by a percentage ΔP based on the local static pressure upstream of the disk. Even though the pressure increase percentage is uniform across the dick, the pressure increase is not due to the non-uniform local static pressure upstream of the disk. The pressure jump across the disk is handled by the approximate Riemann solver in the FASIP code similar to a shock wave.

As mentioned in Section 2, to avoid being divided by 0, the freestream reference condition at Mach number of 0.04 is arbitrarily chosen to be used to normalize the aerodynamic parameters at static conditions. They include $V_\infty = 13.65\ m/s$ and $\rho_\infty = 1.225\ kg/m^3$.

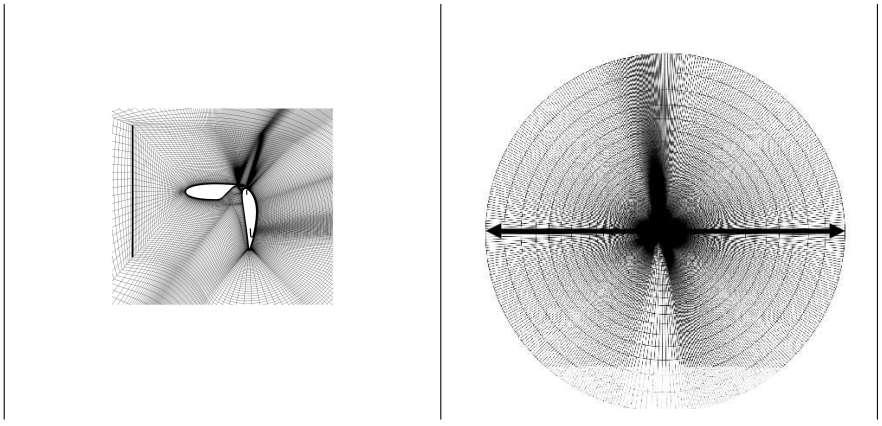

Figure 6: 2D mesh for the deflected slipstream coflow jet airfoil.

4 Results and Discussion

4.1 Validation

Fig. 7 is the double slotted airfoil/wing designed and tested by Kuhn and Draper in 1955 [3] based on NACA 0015 airfoil. The propeller diameter is 1.32 times of the airfoil chord. Fig. 7 (a) is the

cruise condition that the airfoil is retracted. Fig. 7 (b) is the double slotted flaps extended to create the cambering. The deflection angle of each flap element is measured about the chord of the previous element, except that the first element is measured about the horizontal direction. For example, if the deflection angles setup is $\delta = 0°, 40°, 30°$, it means the first element has no deflection, the second element has a deflection angle of 40° about the chord of the first element, and the third element has a deflection angle of 30° about the chord of the second element. The total geometry deflection angel is thus 70°. The testing was done using a slightly tapered wing with two overlapped propellers with disk loading about $40kg/m^2$ [3].

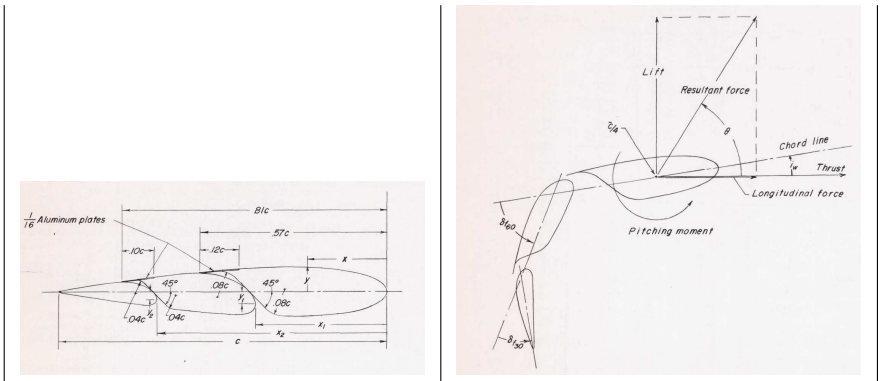

(a) (b)

Figure 7: Baseline slotted airfoil for deflected slipstream with double slotted flaps.

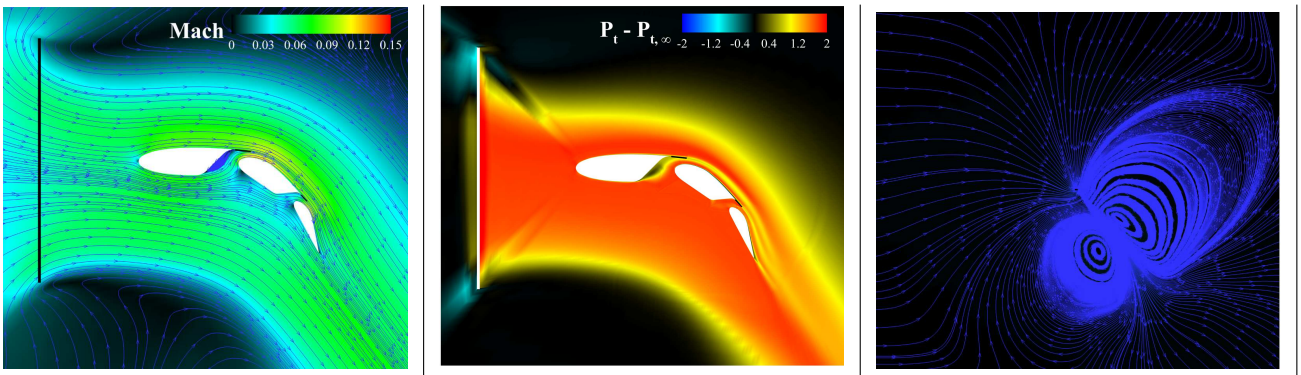

(a) Streamlines (b) Total pressure (c) Farfield Streamlines

Figure 8: Baseline slotted airfoil for deflected slipstream with flap deflection of 0°, 40°, and 30°.

δ_1	δ_2	δ_3	β, measured	β, CFD	L/T, CFD
0°	40°	30°	48.5°	49.33°	68.52%
0°	50°	50°	60.5°	59.52°	73.88%
0°	60°	0°	42°	43.27°	61.29%
0°	70°	30°	64°	42.68°	47.99%

Table 1: Comparison of measured and CFD predicted slipstream deflection for the baseline configuration.

Fig. 8 is the CFD simulated flow field for the baseline configuration of $\delta = 0°$-40°-30° with the same disk loading of the experiment. The dark line on the left is the propeller that pulls the slipstream flow to the right. Fig. 8 (a) shows that the slipstream is well attached and turned by the airfoil, which has a resultant force angle measured as 48.5° in the experiment, significantly less than the geometry deflection

angle of 70°. The CFD predicted angle is 49.33°, a very good agreement with the measurement as shown in Table 1. Fig. 8 (b) shows the total pressure increase due to the work done on the flow by the propeller. Fig. 8 (c) is the streamlines in the static farfield. Since there is no freestream flow, the airfoil force is generated by the propeller that induces two very large counter rotating vortices. The vortex above the suction surface is counter-clockwise and the vortex below the pressure surface is clockwise. These vortices form the circulation around the airfoil that generates the lift. The streamlines in the middle of the two merged vortices is in the opposite direction of the resultant force about 49° as shown in Fig. 8 (a), which is governed by the momentum equation.

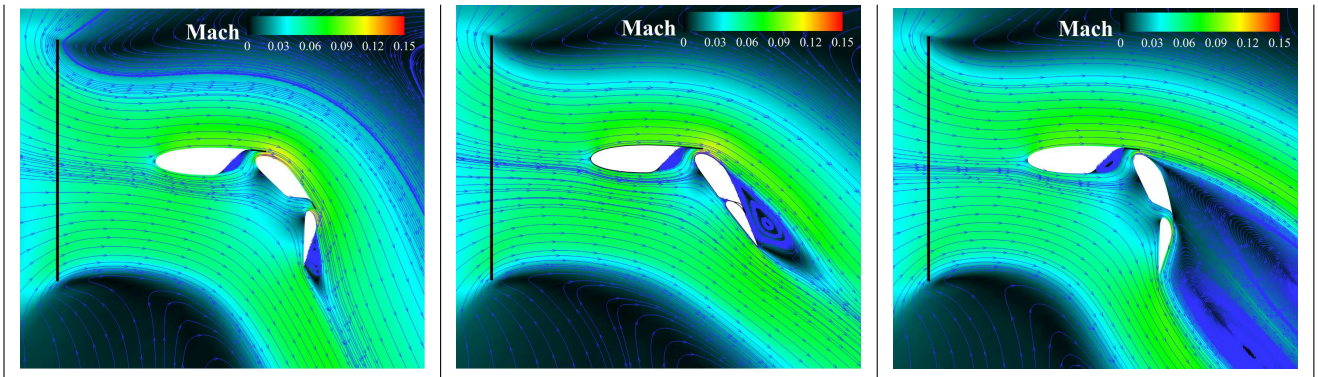

(a) δ = 0°-50°-50° (b) δ = 0°-60°-0° (c) δ = 0°-70°-30°

Figure 9: Baseline slotted airfoil for deflected slipstream at different deflection angles.

Fig. 9 shows the streamlines in the deflection angles of 0°-50°-50°, 0°-60°-0°, and 0°-70°-30°. Fig. 9 (a) has the deflection angle of 100°, but the 3rd element has a flow separation and the whole system has the flow turned by about 60° as shown in Table 1. The configuration of 0°-60°-0° in Fig. 9 (b) has 60° total geometry turning, but only turns the flow by 42° since the flow is largely separated without having a slot between the second and third flap element. The CFD predicts the turning angles of the deflected slipstreams very well for all these cases as shown in Table 9 except the one with δ of 0°-70°-30° in Fig. 9 (c), for which the CFD under-predicts the flow turning with a massive flow separation. The severe flow separation could create a large 3D effect that increases the discrepancy between the experiment and CFD. Overall, as long as there is no massive separation, the CFD predicts the deflected slipstream flow turnings quite well.

4.2 2D Deflected Slipstream Enabled by CoFlow Jet Flap

The good agreement validated with the experiment for the baseline deflected slipstream configurations shown above lays a foundation for further exploration of the deflected slipstream airfoil enabled by coflow jet. At the beginning of the project, we had little experience in applying CFJ on deflected slipstream configurations. The design was thus started with trails and errors based on the same baseline airfoil configuration of Kuhn and Draper [3]. We began with the double slotted baseline airfoil described in the last section and conducted numerous numerical simulations. The flow does not turn with a large separation if the CFJ is applied on the first airfoil element even with very strong jet. It is very effective to apply CFJ on the flaps where a high adverse pressure gradient exists [24]. After a large number of iterations, the final configuration turns out to be very desirable with CFJ applied on a single plain flap, which has the flap chord length of 60% of the total airfoil chord based on NACA 0015 airfoil. Single plain flap is also called simple hinged flap, which has the simplest geometry among flaps.

Fig. 10 shows the Mach numbers contours and streamlines of the three 2D configurations of the DS-CFJ airfoil D242, D244, and D245. All the three flows are nicely attached with injection jet momentum coefficient C_μ of 0.3. It means that the DS-CFJ system can achieve the desired flow turning by a CFJ flap. Table 2 provides some important trends of the configurations and flow performance based on an airfoil planform area of S=1 m^2, δ is the flap deflection angle, β is the resultant force angle about the

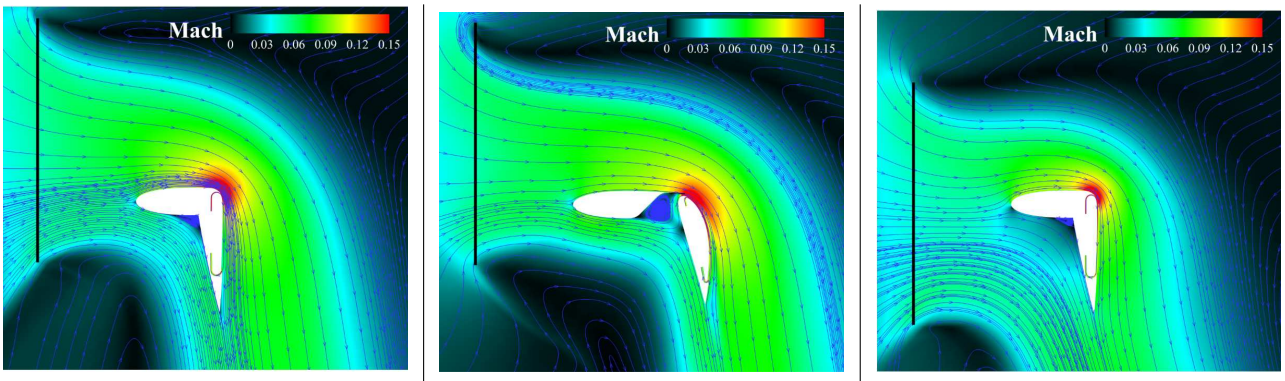

(a) D242: Prop +1/2R (b) D244: Prop +1/2R, slotted (c) D245: Prop in middle

Figure 10: 2D Deflected slipstream airfoil with single plain and slotted flap enabled by coflow jet.

horizontal, and M_j is the injection jet Mach number at the injection slot.

Case	Flap	δ	Prop.	β	L/T	L(N)	D(N)	P_{tot}(kw)	P_{cfj}(kw)	DL(kg/m^2)	FM_{DS}	M_j	Γ
D242	plain	85°	+1/2R	90.02°	105.7%	514.53	0.15	6.53	0.57	37.72	99.3%	0.27	1.017
D244	slotted	82°	+1/2R	85.6°	98.3%	496.71	-38.19	6.97	0.65	39.17	88.3%	0.26	1.020
D245	plain	85°	middle	82.48°	101.19%	490.68	-64.80	6.53	0.59	37.60	92.6%	0.27	1.018

Table 2: Computed DS-CFJ airfoil performance with planform area S=1 m^2, $C_\mu = 0.3$.

As shown by the Mach contours in Fig. 10, all the three configurations have the suction peak at the shoulder of the flap where the flow sharply turns downward from horizontal direction. The velocity is the highest and the pressure is the lowest in that region. The CFJ injection is located at the suction peak region so that a low total pressure would be sufficient to eject the flow at low required power. The flow experiences a severe diffusion with very large adverse pressure gradient after passing the shoulder. At the suction location, the main flow pressure already rises substantially. Placing the suction at a high pressure region near trailing edge also makes the suction only need a low power. Such a CFJ placement in the adverse pressure gradient region creates a low energy expenditure mechanism.

As shown in Eq. (8) and pointed out by Wang and Zha [8, 9], the CFJ power consumption is exponentially proportional to the total pressure ratio and linearly proportional to the mass flow rate. The design guideline for CFJ AFC thus tends to use large injection and suction slot size in order to decrease the total pressure loss and total pressure ratio. Consequently, the mass flow will be increased due to the large injection slot size, but the energy expenditure will be reduced. The mass flow is not an issue for CFJ since it is a ZNMF flow control and all the mass flow is generated locally. In this study, the injection slot size is 0.39%C. The total pressure ratios Γ for all the three cases are no greater than 1.02 as shown in Table 2, which indicates that D242 has the lowest CFJ total pressure ratio as well as the lowest CFJ power required P_{cfj}. Table 2 also indicates that the injection Mach numbers for the 3 configurations are in the range of 0.26-0.27, which are lower than 0.3 and would not be a concern for the jet noise. The low injection Mach number is also benefited form the large injection slot size.

The design D242 shown in Fig. 10 (a) has the airfoil leading edge aligned with the propeller's lower 1/4 diameter position. Such a propeller position pulls more flow to the suction surface of the airfoil and less to the pressure surface. The flap is a single plain flap with a deflection angle of 85°. The coflow jet injection jet strength is $C_\mu = 0.3$. This configuration achieves a 90° flow turning, L/T of 105.7%, and FM_{DS} of 99.3%. The total lift of the D242 configuration is 5.7% greater than the thrust of the propeller. This is because the CFJ enhances the deflected slipstream momentum that contributes to additional lift. The CFJ power is 8.7% of the total hover power. In other words, the propeller disk power of the D242 DS-CFJ system and disk loading are smaller than those of a vertical rotor disk with the same size and the same total lift. The D242's FM_{DS} of 99.3% means that a DS-CFJ system can achieve hover efficiency about the same as a vertical rotor with the same size and same total lift.

The D244 configuration shown in Fig. 10 (b) has the same propeller position and C_μ as those of D242, but uses a slotted single flap that has CFJ applied. The overall performance is significantly deteriorated compared with that of the D242 due to the slot. The flap angle δ is 82°. If δ of 85° is used like D242, the flow will have a small separation at the trailing edge unless a higher C_μ is used. In other words, the D244 configuration is the optimal slotted configuration with C_μ of 0.3. The disk loading and total power are 3.8% and 0.6% higher than those of D242, but the total lift of the DS-CFJ system is 3.5% lower. A flow turning of 85.6° is obtained, 4.4° smaller than that of D242, but is still a very effective angle for VTOL hover. But the overall efficiency FM_{DS} is decreased by 11% compared with D242. This is because the slot creates a flow separation in the gap between the front element and the flap. It also mitigates the pressure load between the pressure and suction surfaces. A slot is advantageous to be used as a passive flow control when the baseline airfoil has high lift loading with flow separation. If we take D242 with single plain flap as the baseline that has no flow separation, the slotted configuration is expected to provide less efficient performance.

To study the effect of propeller position, the D245 configuration has the propeller mounted with its center aligned with the airfoil leading edge as shown in Fig. 10 (c). All other geometry and flow conditions are the same as D242. The performance is also decreased compared with the D242. The resultant force has a vector angle of $\beta = 82.48°$, about 7.5° lower. The total power is the same as that of D242, but the resultant force magnitude (F=$\sqrt{L^2 + D^2}$) is 4% lower. The lift to thrust ratio L/T is 101.19%, indicating the total lift is still higher than the total thrust of the propeller due to the enhanced momentum by the CFJ. The FM_{DS} is 92.6%, better than that of D244, but is 6.7% lower than that of the D242. Overall, a flow turning of 90° for D245 can be achieved by increasing the flap deflection and jet strength of C_μ. It is just not as efficient as D242 with the propeller shifted slightly upward. Comparing Fig. 10 (a) and (c), it is seen that D242 has more mass flow pulled by the propeller on the upper surface that is energized by CFJ. It results in a larger accelerated flow region at the shoulder of of the airfoil when the flow turns. The more energized mass flow on the upper surface with higher momentum pushes the smaller amount of the mass flow from the lower surface and creates a greater flow turning. In fact, the propeller shifted upward by a full radius to be located above the airfoil leading edge provide even larger efficiency and lift gain. However, in reality, placing the propellers on upper surface of the wing may spoil the flow on the suction surface due to the propeller struts. For specific designs, compromise and optimization need to be implemented.

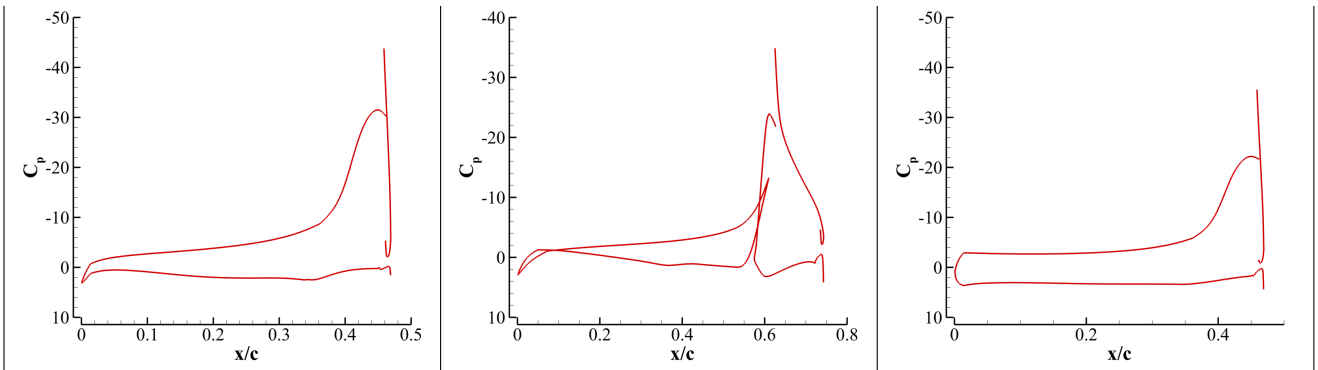

(a) D242: Prop +1/2R (b) D244: Prop +1/2R, slotted (c) D245: Prop in middle

Figure 11: Surface pressure coefficient distributions for the three configurations.

Fig. 11 is the surface pressure coefficient distributions along the airfoil chord x/c. For D242, the flow is rapidly accelerated at the flap hinge position located 40% chord. Consistent with the Mach contours shown in Fig. 10, D242 has substantially higher suction peak than the other two configurations. There is a severe adverse pressure gradient on the flap suction surface with the Cp value varying from about -46 at the flap shoulder to 0 at the trailing edge. From momentum conservation point of view based on the control volume given in Fig. 2, as long as the flow is turned 90°, the resultant force will be all

lift. From the force distribution point of view, the low pressure on the flap suction surface and the high pressure on the flap pressure surface result in a large drag that balances the thrust from the propeller to have the total drag about zero so that β can be 90°.

5 Conclusions

This paper demonstrates numerically that the deflected slipstream enabled by coflow jet active flow control for VTOL hover is feasible based on validated CFD RANS simulation. DS-CFJ airfoil D242 is designed with a single plain flap, 60% flap chord, and deflection angle of 85°. It deflects the slipstream 90° at static condition with a propeller that has a diameter of 1.3 chord and its center positioned with 1/4 diameter above the airfoil leading edge. The deflected slipstream angle is controllable by the flap deflection angle and the jet strength. Two other configurations are presented to show some trends of the DS-CFJ system. They are: 1) D244 with slotted flap and the same propeller position of D242; 2) D245 modified from D242 with the propeller center aligned with the airfoil leading edge. The propeller position of D242 has more flow pulled and energized on the suction surface of the DS-CFJ airfoil by the CFJ. It turns the flow more effectively than positioning the propeller center aligned with the airfoil leading edge. It achieves the best efficiency with FM_{DS} of 99.3%, which basically generates the same lift and consumes the same amount of energy as a conventional vertical rotor with the same size. The total lift generated by D242 is 5.7% greater than the total thrust of the propeller due to the deflected slipstream with enhanced momentum by CFJ. The CFJ power consumption of D242 is about 8.7% of the total power. It means that the propeller of the DS-CFJ system would have 8.7% lower power required than a vertical rotor facing upward to generate the same amount of total lift due to the CFJ contribution. The reduced propeller lift and power required would reduce the disk loading and power loading of the rotor disk, resulting in potentially increased propeller efficiency and reduced noise. The D244 with a slotted flap substantially decreases the efficiency due to the gap that generates a small separation inside and decreases the loading of the airfoil. The D245 with the propeller center aligned with the airfoil leading edge also decreases the efficiency to FM_{DS} of 92.6% because it has more flow on the pressure surface that tends to decrease the turning of the flow from the suction surface. All the injection Mach number is no greater than 0.27 and can be further reduced with optimization. Thus the jet noise is not expected to be a serious concern with the jet Mach number below the noise limit of 0.3 - 0.5. Since a DS-CFJ system avoids the separated flow and large turbulent wakes caused by vertical rotor downwash interaction with the airframe, the broadband noise is expected to be lower.

The DS-CFJ system studied can potentially provide a fully electric powered AAM platform with distributed propulsors and CFJ actuators. It would have the advantages to eliminate tilting wings, tilting rotors, and separate lift-plus-cruise propulsors, and has the potential to improve cruise efficiency, smooth transition, safety, weight reduction, noise mitigation, reliability, maintainability, and passenger acceptance. The feasibility study of this paper enhances our understanding of the DS-CFJ concept, which lays an important foundation for the next step of 3D study and experimental verification.

6 Acknowledgment

The work described in this paper was supported by NASA Langley Research Center's Innovation Fund for Internal Research and Development via National Institute of Aerospace Prime Contract NNL13AA08B, Subcontract No. T16-6500-CJL, Task Order No. 601057. The author gratefully acknowledges Siena K. S. Whiteside and the team at NASA and Coflow Jet, LLC, for their contributions to this activity. Patent Pending.

References

[1] K. R. Antcliff, S. K. Whiteside, L. W. Kohlman, and C. Silva, "Baseline Assumptions and Future Research Areas for Urban Air Mobility Vehicles." AIAA Paper 2019-0528, AIAA SciTech 2019 Forum, San Diego, CA, 7-11 January 2019.

[2] R. E. Kuhn and J. W. Draper, "AN INVESTIGATION OF A WING-PROPELLER CON-

FIGURTION EMPLOYING LARGE-CHORD PLAIN FLAPS AND LARGE-DIAMETER PROPELLERS FOR LOW-SPEED FLIGHT AND VERTICAL TAKE-OFF ." NACA TN-3307, December 1954.

[3] R. E. Kuhn and J. W. Draper, "INVESTIGATION OF EFFECTIVENESS OF LARGE-CHORD SLOTTED FLAPS IN DEFLECTING PROPELLER SLIPSTREAMS DOWNWARD FOR VERTICAL TAKE-OFF AND LOW-SPEED FLIGHT ." NACA TN-3364, Jan. 1955.

[4] R. E. Kuhn, "Investigation of the Effects of Ground Proximity and Propeller Position on the Effectiveness of a Wing with Large-Chord Slotted Flaps in Redirecting Propeller Slipstreams Downward for Vertical Take-Off ." NACA TN-3629, March 1956.

[5] Lefebvre, A. and Zha, G.-C., "Trade Study of 3D Co-Flow Jet Wing for Cruise and Takeoff/Landing Performance." AIAA Paper 2016-0570, AIAA SCITECH2016, AIAA Aerospace Science Meeting, San Diego, CA, 4-8 January 2016.

[6] Yang, Y.-C. and Zha, G.-C., "Super-Lift Coefficient of Active Flow Control Airfoil: What Is the Limit?." AIAA Paper 2017-1693, AIAA SCITECH2017, 55th AIAA Aerospace Science Meeting, Grapevine, Texas, 9-13 January 2017.

[7] Lefebvre, A. and Zha, G.-C. , "Design of High Wing Loading Compact Electric Airplane Utilizing Co-Flow Jet Flow Control." AIAA Paper 2015-0772, AIAA SciTech2015: 53rd Aerospace Sciences Meeting, Kissimmee, FL, 5-9 Jan 2015.

[8] Y. Wang and G.-C. Zha, "Study of 3D Co-flow Jet Wing Induced Drag and Power Consumption at Cruise Conditions." AIAA Paper 2019-0034, AIAA SciTech 2019, San Diego, CA, January 7-11, 2019.

[9] Y. Wang, Y.-C. Yang, and G.-C. Zha, "Study of Super-Lift Coefficient of Co-Flow Jet Airfoil and Its Power Consumption." AIAA Paper 2019-3652, AIAA Aviation 2019, AIAA Applied Aerodynamics Conference, Dallas, Texas, 17-21 June 2019.

[10] Yang, Y.-C. and Zha, G.-C., "Numerical Investigation of Performance Improvement of the Co-Flow Jet Electric Airplane." AIAA Paper 2018-4208, AIAA AVIATION Forum 2018, 2018 Applied Aerodynamics Conference, Atlanta, Georgia, June 25-29, 2018.

[11] Zha, G.-C. and Gao, W. and Paxton, C., "Jet Effects on Co-Flow Jet Airfoil Performance," *AIAA Journal, No. 6,*, vol. 45, pp. 1222–1231, 2007.

[12] G.-C. Zha and D. C. Paxton, "A Novel Flow Control Method for Airfoil Performance Enhancement Using Co-Flow Jet." *Applications of Circulation Control Technologies*, Chapter 10, p. 293-314, Vol. 214, Progress in Astronautics and Aeronautics, AIAA Book Series, Editors: Joslin, R. D. and Jones, G.S., 2006.

[13] Zha, G.-C and Paxton, C. and Conley, A. and Wells, A. and Carroll, B., "Effect of Injection Slot Size on High Performance Co-Flow Jet Airfoil," *AIAA Journal of Aircraft*, vol. 43, 2006.

[14] Zha, G.-C and Carroll, B. and Paxton, C. and Conley, A. and Wells, A., "High Performance Airfoil with Co-Flow Jet Flow Control," *AIAA Journal*, vol. 45, 2007.

[15] Wang, B.-Y. and Haddoukessouni, B. and Levy, J. and Zha, G.-C., "Numerical Investigations of Injection Slot Size Effect on the Performance of Co-Flow Jet Airfoil ," *AIAA Journal of Aircraft*, vol. 45, pp. 2084–2091, 2008.

[16] B. P. E. Dano, D. Kirk, and G.-C. Zha, "Experimental Investigation of Jet Mixing Mechanism of Co- Flow Jet Airfoil." AIAA-2010-4421, (5th AIAA Flow Control Conference, Chicago, IL), 28 Jun - 1 Jul 2010.

[17] B. P. E. Dano, G.-C. Zha, and M. Castillo, "Experimental Study of Co-Flow Jet Airfoil Performance Enhancement Using Micro Discreet Jets." AIAA Paper 2011-0941, 49th AIAA Aerospace Sciences Meeting, Orlando, FL,, 4-7 January 2011.

[18] Lefebvre, A. and Dano, B. and Bartow, W. and Di Franzo, M. and Zha, G.-C., "Performance and Energy Expenditure of Co-Flow Jet Airfoil with Variation of Mach Number," *AIAA Journal of Aircraft*, vol. 53, pp. 1757–1767, 2016.

[19] Lefebvre, A. and Zha, G.-C., "Numerical Simulation of Pitching Airfoil Performance Enhancement Using Co-Flow Jet Flow Control." AIAA Paper 2013-2517, AIAA Applied Aerodynamics Conference, San Diego, CA, 24 - 27 June 2013.

[20] Liu, Z.-X. and Zha, G.-C., "Transonic Airfoil Performance Enhancement Using Co-Flow Jet Active Flow Control." AIAA Paper 2016-3472, AIAA AVIATION 2016, 8th AIAA Flow Control Conference, Washington, D.C, June 13-17, 2016.

[21] K.-W. Xu and G.-C. Zha, "High control authority 3d aircraft control surfaces using co-flow jet," *AIAA Journal of Aircraft*, July 2020.

[22] Xu, Kewei and Zha, Gecheng, "System energy benefit using co-flow jet active separation control for a serpentine duct," *Elsevier Journal of Aerospace Science and Technology*, vol. 128, p. DOI: 10.1016/j.ast.2022.107746, 2022.

[23] Xu, Kewei and Ren, Yan and Zha, Gecheng, "Numerical Analysis of Energy Expenditure for Co-Flow Wall Jet Separation Control ," *AIAA Journal*, vol. 60, no. 5, p. doi.org/10.2514/1.J061015, 2022.

[24] Xu, Kewei and Zha, Gecheng, "Enhancing aircraft control surface effectiveness by co-flow jet flap at low energy expenditure ," *Elsevier Journal of Aerospace Science and Technology*, vol. 133, 2023.

[25] G.-C. Zha, Y.-C. Yang, Y. Ren, and B. McBreen, "Super-lift and thrusting airfoil of coflow jet-actuated by micro-compressors." AIAA Paper 2018-3061, AIAA AVIATION 2018, Atlanta, GA , 25 - 29 June 2018.

[26] K.-W. Xu, Y. Ren, and G.-C. Zha, "Separation control by coflow wall jet." AIAA Paper 2021-2946, AIAA Aviation 2021, Virtual Event, 2-6 Aug. 2021.

[27] B. McBreen, K.-W. Xu, and and Zha, G.-C., "Numerical Study of Extreme Adverse Pressure gradients Enabled by Co-Flow Jet." AIAA Paper 2023-1430, AIAA 2023 SciTech Forum, National Harbor, MD , 23-27 Jan. 2023.

[28] K. Xu and G. Zha, "Design of high specific speed mixed flow micro-compressor for co-flow jet actuators." ASME Paper GT-2019-90980, ASME IGTI Turbo Expo 2019, Phoenix, Arizona, USA, June 17 - 21, 2019.

[29] Barrios, P. A. and Ren, Y. and Zha, G.-C., "Simulation of 3D Co-Flow Jet Airfoil with Integrated Micro-Compressor Actuator at Different Cruise Mach Numbers." AIAA Paper 2023-2118, 2023 AIAA SciTech Forum, National Harbor, MD, Jan 23-27, 2023.

[30] Ren, Y. and Barrios, P. A. and Zha, G.-C., "Simulation of 3D Co-Flow Jet Airfoil with Integrated Micro-Compressor Actuator." AIAA Paper 2022-3553, AIAA AVIATION Forum, Chicago, IL & Virtual , June 27-July 1, 2022.

[31] P. Spalart and S. Allmaras, "A One-equation Turbulence Model for Aerodynamic Flows." AIAA-92-0439, 1992.

[32] G.-C. Zha and E. Bilgen, "Numerical Solutions of Euler Equations by Using a New Flux Vector Splitting Scheme ," *International Journal for Numerical Methods in Fluids*, vol. 17, pp. 115–144, 1993.

[33] Shen, Y.-Q. and Zha, G.-C. and Chen, X.-Y., " High Order Conservative Differencing for Viscous Terms and the Application to Vortex-Induced Vibration Flows," *Journal of Computational Physics*, vol. 228(2), pp. 8283–8300, 2009.

[34] Y.-Q. Shen and G.-C. Zha, "Large Eddy Simulation Using a New Set of Sixth Order Schemes for Compressible Viscous Terms ," *Journal of Computational Physics*, vol. 229, pp. 8296–8312, 2010.

[35] G.-C. Zha, Y. Shen, and B. Wang, "An improved low diffusion E-CUSP upwind scheme ," *Journal of Computer & Fluids*, vol. 48, pp. 214–220, 2011.

[36] G. C. Zha, D. Smith, M. Schwabacher, K. Rasheed, A. Gelsey, and D. Knight, "High Performance Supersonic Missile Inlet Design Using Automated Optimization." AIAA Paper 96-4142, 1996.

[37] X.-Y. Chen and G.-C. Zha, "Fully Coupled Fluid-Structural Interactions Using an Efficient High Solution Upwind Scheme." AIAA Paper 2004-2331, to appear in Journal of Fluids and Structures, 2005.

[38] B.-Y. Wang and G.-C. Zha, "A General Sub-Domain Boundary Mapping Procedure For Structured Grid CFD Parallel Computation," *AIAA Journal of Aerospace Computing, Information, and Communication*, vol. 5, No.11, pp. 2084–2091, 2008.

[39] K.-W. Xu and G.-C. Zha, "Mitigation of Serpentine Duct Flow Distortion Using CoFlow Jet Active Flow Control ." AIAA-2020-2954, AIAA Aviation 2020 Virtual Forum, 15-19 June, 2020.